Advances in Applied Mathematics and Mechanics
Adv. Appl. Math. Mech., Vol. **15**, No. 1, pp. 182-201

DOI: 10.4208/aamm.OA-2021-0197
February 2023

Localized Method of Fundamental Solutions for Acoustic Analysis Inside a Car Cavity with Sound-Absorbing Material

Zengtao Chen[1] and Fajie Wang[1,2,*]

[1] *College of Mechanical and Electrical Engineering, National Engineering Research Center for Intelligent Electrical Vehicle Power System, Qingdao University, Qingdao, Shandong 266071, China*
[2] *Institute of Mechanics for Multifunctional Materials and Structures, Qingdao University, Qingdao, Shandong 266071, China*

Received 8 June 2021; Accepted (in revised version) 20 September 2021

Abstract. This paper documents the first attempt to apply a localized method of fundamental solutions (LMFS) to the acoustic analysis of car cavity containing sound-absorbing materials. The LMFS is a recently developed meshless approach with the merits of being mathematically simple, numerically accurate, and requiring less computer time and storage. Compared with the traditional method of fundamental solutions (MFS) with a full interpolation matrix, the LMFS can obtain a sparse banded linear algebraic system, and can circumvent the perplexing issue of fictitious boundary encountered in the MFS for complex solution domains. In the LMFS, only circular or spherical fictitious boundary is involved. Based on these advantages, the method can be regarded as a competitive alternative to the standard method, especially for high-dimensional and large-scale problems. Three benchmark numerical examples are provided to verify the effectiveness and performance of the present method for the solution of car cavity acoustic problems with impedance conditions.

AMS subject classifications: 65N80, 62P30, 35J05

Key words: Acoustic analysis, localized method of fundamental solutions, car cavity, sound-absorbing material.

1 Introduction

Acoustic analysis plays a significant role in many fields such as vehicle noise control [1, 2] and indoor sound insulation [3, 4]. In recent years, a large amount of research [5–8] has been devoted to the acoustic analysis and simulation in practical engineering and

*Corresponding author.
Email: wfj1218@126.com (F. Wang)

industry fields. In the numerical algorithms, the finite element method (FEM) [9, 10], finite difference method (FDM) [11] and boundary element method (BEM) [12] are the most common methods in the simulation and calculation of interior acoustics field. At present, the FEM and the BEM have been considered as powerful tools for numerical simulation of acoustic problems. However, these approaches are difficult to avoid the tasks of mesh generation and numerical integration, which is often very time-consuming and tedious, especially for high-dimensional and complex geometries.

Over the last few decades, many efforts have been made to develop new numerical schemes in order to reduce or completely avoid gridding as well as numerical integration. Various meshfree methods or meshless methods [13–17] have been presented and applied to the acoustic analysis. These methods can be roughly classified into two categories, namely, boundary-type methods and domain-type methods. The former mainly includes the method of fundamental solutions (MFS) [18–21], the boundary knot method (BKM) [22, 23], the singular boundary method (SBM) [24, 25] and so on. The latter includes the generalized finite difference method (GFDM) [26,27], the element-free Galerkin method (EFGM) [28, 29], the radial basis function collocation method (RBFCM) [30] and so on. For details on advance and application of meshless method, the readers can refer to [31–33] and references therein.

To overcome the bottleneck that the boundary-type method with global discretization is difficult to apply to large-scale problems, recently, the localized versions of the boundary-type meshless methods including the MFS, the BKM and the SBM have been proposed. Wang et al. [15, 16, 34, 35] presented the localized BKM (LBKM) for simulating convection-diffusion-reaction problem and acoustics problem. Liu and Fan et al. [36] developed the localized Trefftz method and applied it to numerical solutions of Laplace equation and biharmonic equation. Xi and Fu et al. [37] presented a localized collocation Trefftz method for heat conduction analysis in two kinds of heterogeneous materials (functionally graded materials and multi-medium materials) under temperature loading. Wang et al. proposed a localized SBM and a localized Chebyshev collocation method [38, 39]. Fan and Chen et al. [40] proposed the localized MFS (LMFS) for solving boundary value problems governed by Laplace equation and biharmonic equation. Very recently, Gu, Wang, Li et al. [41–45] applied the LMFS to the elastic wave, diffusion, inverse problem, heat conduction problem and so on. Qu et al. [46, 47] made a first attempt to employ the LMFS to simulate three-dimensional (3D) interior acoustic fields at low frequency as well as two-dimensional (2D) interior Helmholtz problems with high wave number. In their works, however, the closed space with a sound absorbing material has not been considered, which is a common issue in many applications. Moreover, the investigation of the LMFS in the acoustic analysis of car cavity with impedance condition has not been reported yet.

In this paper, the LMFS is firstly implemented to predict the sound field in a car cavity with impedance boundary conditions and medium-low frequencies. The LMFS is free from numerical integration and mesh generation. Only some regularly or irregularly distributed nodes are required both inside the physical domain and on its boundary.

Since the car cavity often contains sound-absorbing material, the impedance boundary condition is introduced to acoustic model for characterizing the sound absorption characteristics. Numerical experiments including 2D and 3D models are presented to demonstrate the effectiveness of the proposed algorithm. Furthermore, the FEM results obtained from COMSOL Multiphysics 5.4 are employed to test the performance of the developed method in the acoustic analysis of car cavity with impedance boundary condition.

2 Problem statement

Assuming that the sound propagates in uniform air, the following Helmholtz equation can be considered to describe acoustic field distribution inside a car cavity (Ω):

$$\nabla^2 p + k^2 p = 0, \tag{2.1}$$

in which, $k(=\omega/c)$ is the wave number with ω being the angular frequency and c being the sound speed in the acoustic medium, and p represents the sound pressure.

The acoustic problem of car cavity usually involves the following three kinds of boundary conditions:

$$p = p_D \qquad \text{on } \Gamma_D, \tag{2.2a}$$
$$\nabla p \cdot \boldsymbol{n} = -j\rho\omega v_n \qquad \text{on } \Gamma_N, \tag{2.2b}$$
$$\nabla p \cdot \boldsymbol{n} = -j\rho\omega A_n p \qquad \text{on } \Gamma_R, \tag{2.2c}$$

where ρ is the mass density, $j=\sqrt{-1}$, $\boldsymbol{n}$ is the outward normal vector. Γ_D, Γ_N and Γ_R respectively are boundary parts corresponding to Dirichlet, Neumann and Robin boundary conditions. p_D and v_n are known values of the sound pressure on Γ_D and the normal velocity on Γ_N, A_n represents the acoustic admittance on Γ_R.

3 The LMFS for acoustic analysis of car cavity

According to the ideas of the LMFS, $N=ni+nd+nn+nr$ nodes x^i $(i=1,\cdots,N)$ are placed over the physical domain, where ni represents the number of interior nodes, nd, nn and nr is the numbers of boundary nodes along the Dirichlet, Neumann and Robin boundary segments, respectively. Taking the 3D case as an example [48], we can find m supporting nodes $x^{(i)}$ $(i=1,\cdots,m)$ around the central node $x^{(0)}$ (see Fig. 1). At the same time, the local subdomain Ω_s can also be defined. Subsequently, the MFS formulation is implemented on the local subdomain. Fig. 2(a) shown the artificial boundary $\widehat{\Omega}_s$, which is selected at a certain distance from the boundary of local subdomain. On the artificial boundary, M uniformly distributed source points are specified (see Fig. 2(b)).

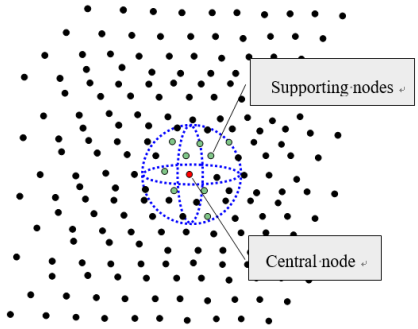

Figure 1: The sketch of the LMFS.

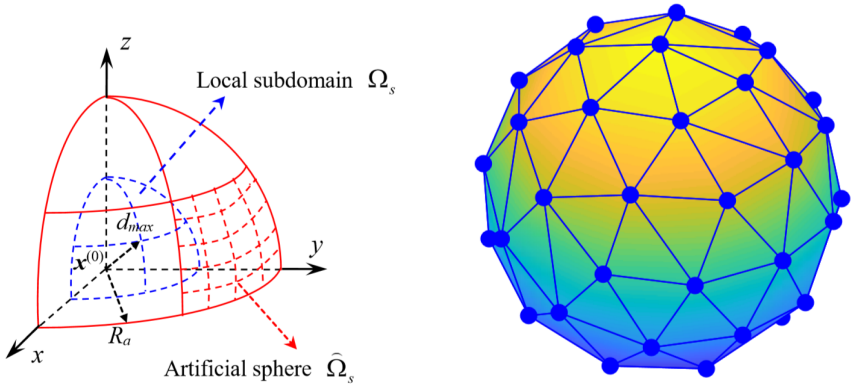

(a) Artificial sphere (b) Distribution of source points

Figure 2: The schematic diagram for (a) the artificial sphere associated with Ω_s, and (b) M source points uniformly distributed along the artificial sphere surface.

For each node in the local subdomain Ω_s, the MFS formulation of sound pressure can be expressed as

$$p(\boldsymbol{x}^{(i)}) = \sum_{j=1}^{M} G(\boldsymbol{x}^{(i)}, \boldsymbol{s}^{(j)})\beta_j, \quad \boldsymbol{x}^{(i)} \in \Omega_s, \quad i = 0,1,\cdots,m, \tag{3.1}$$

or for brevity

$$p^{(i)} = \sum_{j=1}^{M} G_{ij}\beta_j = \boldsymbol{G}^{(i)}\boldsymbol{\beta}, \quad \boldsymbol{x}^{(i)} \in \Omega_s, \quad i = 0,1,\cdots,m, \tag{3.2}$$

in which, $(\boldsymbol{s}^{(j)})_{j=1}^{M}$ represent M fictitious source points, $(\boldsymbol{x}^{(i)})_{i=0}^{m}$ are the $m+1$ collocation points in the subdomains Ω_s, $\boldsymbol{\beta} = (\beta_1, \beta_2, \cdots, \beta_M)^{\mathrm{T}}$ is the unknown coefficient vector, $G_{ij} =$

$G(\boldsymbol{x}^{(i)},\boldsymbol{s}^{(j)})$ can be expressed as

$$G(\boldsymbol{x}^{(i)},\boldsymbol{s}^{(j)})=\frac{e^{ik\left\|\boldsymbol{x}^{(i)}-\boldsymbol{s}^{(j)}\right\|_2}}{4\pi\left\|\boldsymbol{x}^{(i)}-\boldsymbol{s}^{(j)}\right\|_2}. \tag{3.3}$$

In each local subdomain, the residual function can be defined as follows

$$B(p)=\sum_{i=0}^{m}\left[\boldsymbol{G}^{(i)}\boldsymbol{\beta}-p^{(i)}\right]^2\omega^{(i)}, \tag{3.4}$$

where $\omega^{(i)}$ is the weighting function associated with node $x^{(i)}$ and is presented as [49]

$$\omega^{(i)}=\frac{\exp\left[-(d_i/h)^2\right]-\exp\left[-(d_{\max}/h)^2\right]}{1-\exp\left[-(d_{\max}/h)^2\right]},\quad i=0,1,\cdots,m, \tag{3.5}$$

in which $d_i=\|\boldsymbol{x}^{(i)}-\boldsymbol{x}^{(0)}\|$ is the distance between the central node $x^{(0)}$ and the ith supporting node, $d_{\max}=\max_{i=1,\cdots,m}(d_i)$ indicates the radius of the local subdomain, and $h=1$. It should be pointed out that the radius of artificial domain is $R_a=R_S d_{\max}$ (see Fig. 2(a)), here $R_S>1$ is a parameter that can be determined manually.

According to the theory of moving least square (MLS) method, the unknown coefficients $\boldsymbol{\beta}=(\beta_1,\beta_2,\cdots,\beta_M)^T$ can be decided by minimizing the functional $B(p)$, thus

$$\frac{\partial B(p)}{\partial\beta_j}=0,\quad j=1,\cdots,M. \tag{3.6}$$

Then, the following local linear system can be formed

$$\boldsymbol{A}\boldsymbol{\beta}=\boldsymbol{b}, \tag{3.7}$$

where

$$\boldsymbol{A}=\begin{bmatrix}\sum\limits_{i=0}^{m}G_{i1}^2\omega^{(i)} & \sum\limits_{i=0}^{m}G_{i1}G_{i2}\omega^{(i)} & \sum\limits_{i=0}^{m}G_{i1}G_{i3}\omega^{(i)} & \cdots & \sum\limits_{i=0}^{m}G_{i1}G_{iM}\omega^{(i)}\\ & \sum\limits_{i=0}^{m}G_{i2}^2\omega^{(i)} & \sum\limits_{i=0}^{m}G_{i2}G_{i3}\omega^{(i)} & \cdots & \sum\limits_{i=0}^{m}G_{i2}G_{iM}\omega^{(i)}\\ & & \sum\limits_{i=0}^{m}G_{i3}^2\omega^{(i)} & \cdots & \sum\limits_{i=0}^{m}G_{i3}G_{iM}\omega^{(i)}\\ & SYM & & \ddots & \vdots\\ & & & & \sum\limits_{i=0}^{m}G_{iM}^2\omega^{(i)}\end{bmatrix},\quad \boldsymbol{b}=\begin{bmatrix}\sum\limits_{i=0}^{m}G_{i1}\omega^{(i)}p^{(i)}\\ \sum\limits_{i=0}^{m}G_{i2}\omega^{(i)}p^{(i)}\\ \sum\limits_{i=0}^{m}G_{i3}\omega^{(i)}p^{(i)}\\ \vdots\\ \sum\limits_{i=0}^{m}G_{iM}\omega^{(i)}p^{(i)}\end{bmatrix}, \tag{3.8a}$$

$$\boldsymbol{b}=\begin{bmatrix}G_{01}\omega^{(0)} & G_{11}\omega^{(1)} & \cdots & G_{m1}\omega^{(m)}\\ G_{02}\omega^{(0)} & G_{12}\omega^{(1)} & \cdots & G_{m2}\omega^{(m)}\\ \vdots & \vdots & \ddots & \vdots\\ G_{0M}\omega^{(0)} & G_{1M}\omega^{(1)} & \cdots & G_{mM}\omega^{(m)}\end{bmatrix}\begin{pmatrix}p^{(0)}\\ p^{(1)}\\ \vdots\\ p^{(m)}\end{pmatrix}=\boldsymbol{B}\begin{pmatrix}p^{(0)}\\ p^{(1)}\\ \vdots\\ p^{(m)}\end{pmatrix}. \tag{3.8b}$$

The unknown coefficients $\boldsymbol{\beta}=(\beta_1,\beta_2,\cdots,\beta_M)^T$ can be calculated from Eqs. (3.7)-(3.8b)

$$\boldsymbol{\beta}=\begin{pmatrix}\beta_1\\ \beta_2\\ \vdots\\ \beta_M\end{pmatrix}=\boldsymbol{A}^{-1}\boldsymbol{B}\begin{pmatrix}p^{(0)}\\ p^{(1)}\\ \vdots\\ p^{(m)}\end{pmatrix}. \tag{3.9}$$

To guarantee the regularity of matrix $\boldsymbol{A}$ in Eq. (3.9), M should be lesser than $m+1$. In general, we fixed $m+1=2M$ in the computations.

The sound pressure at the central node $x^{(0)}$ can be obtained by combining Eqs. (3.9) and (3.2):

$$p^{(0)}=\boldsymbol{G}^{(0)}\boldsymbol{\beta}=\boldsymbol{G}^{(0)}\boldsymbol{A}^{-1}\boldsymbol{B}\begin{pmatrix}p^{(0)}\\ p^{(1)}\\ \vdots\\ p^{(m)}\end{pmatrix}=\sum_{j=0}^{m}c^{(j)}p^{(j)}, \tag{3.10}$$

or

$$p^{(0)}-\sum_{j=0}^{m}c^{(j)}p^{(j)}=0, \tag{3.11}$$

where $(c^{(j)})_{j=0}^{m}$ are coefficients. The above procedure should be repeated for every node inside the physical domain, and the sound pressure at every node can be expressed in the form of Eq. (3.11).

Now, the final system of linear algebraic equations can be formed. In the computational domain, internal nodes must satisfy the control equation, and all boundary nodes satisfy the boundary conditions. Finally, a large sparse linear equation system is formed, and the physical quantities at all points in the calculation domain can be obtained by solving the equation system. At interior nodes, the physical quantities must satisfy the acoustic control equation, and the following equations should also be satisfied

$$p^{(i)}-\sum_{j=0}^{m}c_i^{(j)}p^{(j)}=0,\quad i=1,\cdots,n_i, \tag{3.12}$$

in which subscript i indicates the differences between different nodes. Then, the nodes with Dirichlet boundary conditions should be satisfied

$$p^{(i)}=p_D,\quad i=n_i+1,n_i+2,\cdots,n_i+n_d, \tag{3.13}$$

And then, the following equations can be obtained from Neumann boundary conditions

$$\nabla p^{(i)}\cdot\boldsymbol{n}=-j\rho\omega v_n,\quad i=n_i+n_d+1,n_i+n_d+2,\cdots,n_i+n_d+n_n, \tag{3.14}$$

or

$$\nabla p^{(i)}\cdot\boldsymbol{n}=\frac{\partial p^{(i)}}{\partial n}=\sum_{j=1}^{M}\frac{\partial G(\boldsymbol{x}^{(i)},\boldsymbol{s}^{(j)})}{\partial n}\beta_j=\frac{\partial \boldsymbol{G}^{(i)}}{\partial n}\boldsymbol{\beta}$$
$$=\frac{\partial \boldsymbol{G}^{(i)}}{\partial n}\boldsymbol{A}^{-1}\boldsymbol{B}\begin{pmatrix}p^{(0)}\\ p^{(1)}\\ \vdots\\ p^{(m)}\end{pmatrix}=-j\rho\omega v_n, \tag{3.15}$$

in which $\boldsymbol{n}=(n_1^i,n_2^i)$ is the normal vector in the x direction and y direction, respectively. Finally, the following equations should be satisfied from Robin boundary conditions

$$\nabla p^{(i)}\cdot\boldsymbol{n}=-j\rho\omega A_n p^{(i)},\quad i=n_i+n_d+n_n+1,n_i+n_d+n_n+2,\cdots,N, \tag{3.16}$$

or

$$\nabla p^{(i)}\cdot\boldsymbol{n}=\frac{\partial p^{(i)}}{\partial n}=\sum_{j=1}^{M}\frac{\partial G(\boldsymbol{x}^{(i)},\boldsymbol{s}^{(j)})}{\partial n}\beta_j=\frac{\partial \boldsymbol{G}^{(i)}}{\partial n}\boldsymbol{\beta}$$
$$=\frac{\partial \boldsymbol{G}^{(i)}}{\partial n}\boldsymbol{A}^{-1}\boldsymbol{B}\begin{pmatrix}p^{(0)}\\ p^{(1)}\\ \vdots\\ p^{(m)}\end{pmatrix}+j\rho\omega A_n p^{(i)}=0. \tag{3.17}$$

Using the given boundary conditions and combining Eqs. (3.12)-(3.17), a sparse system of linear algebraic equations can be produced as follows

$$\boldsymbol{CP}=\boldsymbol{f}, \tag{3.18}$$

where $\boldsymbol{C}_{N\times N}$ denotes the coefficient matrix, $\boldsymbol{P}=(p^{(1)},p^{(2)},\cdots,p^{(N)})^{\mathrm{T}}$ represents a column vector with components being unknown variables at every nodes, and $\boldsymbol{f}_{N\times 1}$ is a known vector composed by given boundary conditions and zero vector. It should be pointed out that the system given in Eq. (3.18) is well-conditioned, and standard solvers can be used to obtain its solution. In this study, the MATLAB routine "$\boldsymbol{P}=\boldsymbol{C}\backslash\boldsymbol{f}$" is used to solve this system of equation. After solving Eq. (3.18), the numerical results of $p(x^{(i)})$ at every node can be acquired.

4 Numerical results and discussions

In the following, three benchmark numerical examples are provided to verify the feasibility of the above-mentioned methodology. It should be pointed out that the medium in the cavity is air for all the tested examples. The air density ρ is 1.225kg/m^3 and the sound

speed c in the air is 343m/s. In Examples 4.2 and 4.3, the nodes in the model are derived from the HyperMesh software. To save space and avoid repetition, these parameters will not be indicated again later. In all calculations, the parameter of artificial radius are fixed with $R_s=1.5$ for 2D case and $R_s=20$ for 3D case, and the numerical results are calculated on a computer equipped with i5-5200 CPU@2.20GHz and 4GB memory.

It should be stated that the sound pressure (p) in Example 4.1 means the imaginary part of sound pressure, and it means the real part of sound pressure in Examples 4.2 and 4.3. The sound pressure level (SPL) is defined as

$$SPL=20\log_{10}\left(\frac{p_{rms}}{p_0}\right), \tag{4.1}$$

where p_{rms} denotes the root-mean-square pressure and $p_0=2\times10^{-5}$Pa is the reference pressure. For a pure-tone excitation, p_{rms} is equal to

$$p_{rms}=\frac{p}{\sqrt{2}}, \quad p=\sqrt{p_{re}^2+p_{im}^2}, \tag{4.2}$$

where p is the pressure amplitude, p_{re} and p_{im} are the real and imaginary parts of the sound pressure, respectively.

To estimate the accuracy of the present scheme, we adopt the root-mean-square error $(RMSE)$, relative error defined by

$$RMSE=\sqrt{\frac{1}{N_{total}}\sum_{k}^{N_{total}}\left(p_{num}(\boldsymbol{x}^k)-p_{exa}(\boldsymbol{x}^k)\right)^2}, \tag{4.3a}$$

$$Relative\ \ error=\left|\frac{p_{num}(\boldsymbol{x}^k)-p_{exa}(\boldsymbol{x}^k)}{p_{exa}(\boldsymbol{x}^k)}\right|, \tag{4.3b}$$

where $p_{num}(\boldsymbol{x}^k)$ and $p_{exa}(\boldsymbol{x}^k)$ are the numerical and analytical solutions at kth test points respectively, N_{total} is the total number of tested points, which refers to all nodes unless otherwise specified.

4.1 Two-dimensional rectangular cavity

First of all, a benchmark acoustic model is employed to verify the accuracy, stability and convergence of the LMFS in solving the 2D acoustic problem. Fig. 3 shows the sketch of acoustic model. The normal velocity on the left boundary is given as $v_n=0.01$m/s and the acoustic admittance on the right boundary is given as $A_n=0.00144$m/(Pa·s), the remaining part are acoustic hard boundary. The exact solution of this problem is available, and the distribution of sound pressure inside the cavity can be expressed by

$$P=-j\rho\omega v_n\frac{\cos(k(1-x))}{\sin k}. \tag{4.4}$$

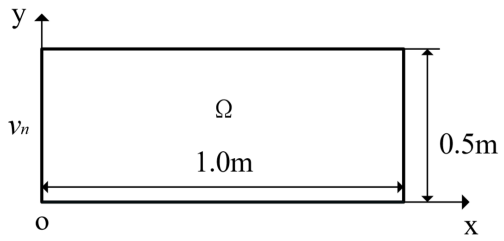

Figure 3: A 2D rectangular cavity.

In the driving process, the most frequent contact is the medium-low frequencies noise (200-500Hz) [50–52]. Consequently, we first consider the calculation results at frequency $f=400$Hz, and numerically analyze the relationship between supporting nodes m and node spacing Δh (noted that the node spacing is equivalent to the total number of nodes). Without loss of generality, the node spacing is defined by

$$\Delta h=\max_{1\le i\le N}\min_{1\le j\le N}\left|\boldsymbol{x}_i-\boldsymbol{x}_j\right|.$$

Following the ideas in [53,54], Fig. 4 illustrates profiles of $RMSEs$ from the LMFS with respect to various values of m and Δh. It can be observed from Fig. 4(a) that the calculation accuracy of the LMFS under different parameters m and Δh. Furthermore, we can plot a fitting curve (see Fig. 4(b)) passing through the red points ($RMSE=1.0e-02$). From this curve, the following empirical formula can be formulated for estimating the relatively optimal number of supporting nodes:

$$m=\left\lceil 6.6\cdot\Delta h^{(-0.24)}\right\rceil. \tag{4.5}$$

To carefully validate the efficiency and stability of the developed method, Table 1 compares the relative error obtained by the LMFS, GFDM and FEM. In our calculation, the LMFS and GFDM have the same parameter conditions, which means $N=1{,}246$ ($\Delta h=$ 0.02m). It can be known from the empirical formula (4.5) that the number of supporting nodes need to meet $m\ge 17$, when the numerical error remains $RMSE\le 1.0e-02$. Hence, m is set as 17 in the LMFS procedure. In the FEM simulation, the model is discretized into 4,270 nodes, included 4,030 domain elements. It can be found from Table 1, the proposed LMFS can achieve more accurate and stable numerical results compared with the GFDM under the same number of nodes. In addition, the accuracy of the proposed method is higher than that of the FEM, in which the former uses relatively few nodes. It also shows the potential of this algorithm in reducing the memory consumption and improving the efficiency of numerical calculation.

To investigate the effect of the radius of the artificial domain (R_a) on the numerical accuracy, Fig. 5 shows the numerical results obtained by using the LMFS with different parameters ($R_S=1.5,2,2.5,3$). It can be observed that the proposed method is accurate

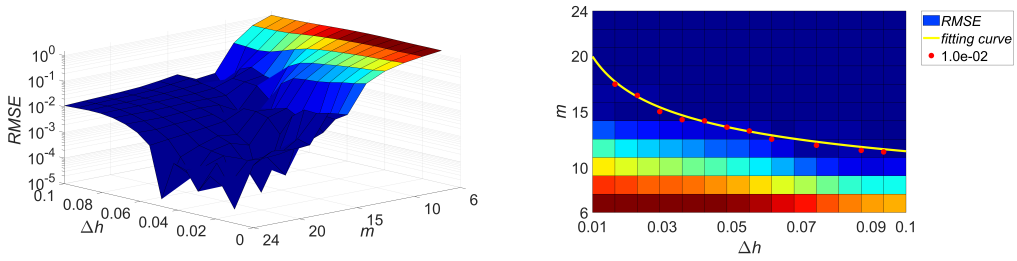

(a) 3D error surface (b) 2D error plane

Figure 4: Error distributions of the LMFS at $f=400$Hz.

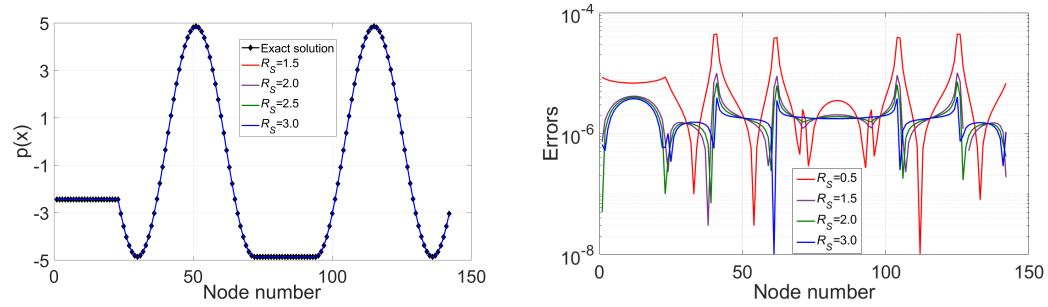

(a) Numerical solutions (b) Relative errors

Figure 5: The LMFS results and relative errors on boundary nodes under different parameters of artificial radius.

and stable for various values of R_S, and is completely insensitive to the change of the parameter R_S. For simplicity, $R_S=1.5$ is adopted in all tested examples associated with 2D problems.

In order to verify the convergence of the presented method at different frequencies, we investigate the influence of the total number of nodes (N) and the number of supporting nodes (m) on the LMFS solutions. Fig. 6(a) and Fig. 6(b) show error curves with increasing numbers of total nodes and supporting nodes, respectively. From Fig. 6(a), we can see that the proposed approach is fast convergent with respect to the total number of nodes. It is noted from Fig. 6(b) that the $RMSE$ first decreases and then tends to a con-

Table 1: Relative errors of the LMFS, GFDM and FEM under $f=400$Hz.

Test points	LMFS	GFDM	FEM
$(0.2,0)$	$1.085e-04$	$1.009e-02$	$9.221e-03$
$(0.4,0)$	$4.303e-04$	$1.397e-02$	$9.027e-02$
$(0.6,0)$	$1.303e-04$	$1.075e-02$	$1.475e-02$
$(0.8,0)$	$8.168e-04$	$2.617e-02$	$9.155e-02$
$(1.0,0)$	$1.844e-04$	$9.199e-03$	$1.661e-02$

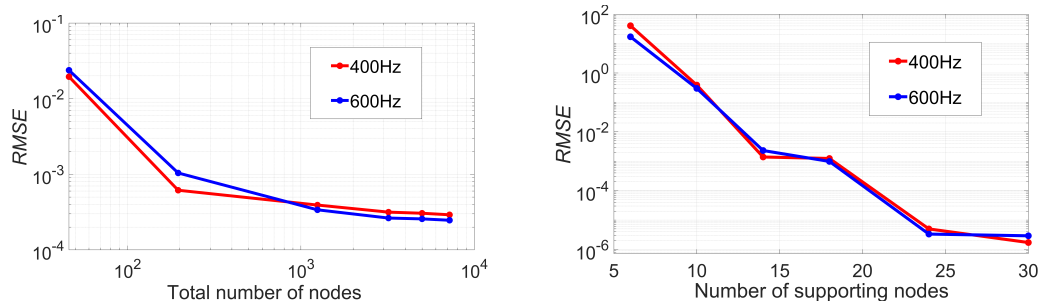

(a) RMSE against the total number of nodes (b) RMSE against the number of supporting nodes

Figure 6: Error curves of the LMFS under different frequencies with respect to (a) the total number of nodes ($m=20$) and (b) the number of source points ($N=4{,}996$).

stant basically with increasing number of supporting nodes. In fact, an accurate solution can be achieved even if the value of m is taken as a relatively smaller one, such as 14 and 16.

4.2 Two-dimensional car cavity with impedance boundary

In this example, the LMFS is applied to the acoustic analysis of a 2D car cavity with impedance boundary condition. Fig. 7 shows acoustic models of car cavities with and without seats, here model A and model B have the same size. The length of the car cavity is $L=2.65$m, and the width $H=1.12$m. Considering the main part of vehicle noise is caused from the engine, the normal velocity $v_n=0.01\text{m/s}$ is imposed on the front wall of the car. The top of the car cavity is usually made of sound-absorbing material, and thus the boundary "cd" is specified as the Robin boundary condition with the acoustic admittance $A_n=0.00144\text{m}/(\text{Pa}\cdot\text{s})$, the remaining part is set to the acoustic hard boundary condition. In the simulation, the numerical results at the bottom boundary "ab" are obtained and shown for indicating the performance of the algorithm.

Since no analytical solution is available for this example, our simulation results are compared with the FEM solutions obtained from COMSOL. In the calculation, the finite

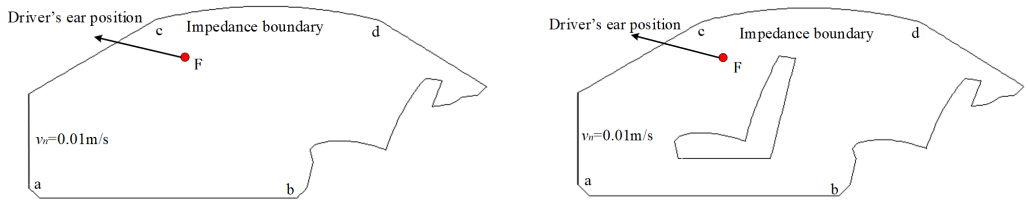

(a) Model A without seat (b) Model B with seat

Figure 7: 2D car cavities with impedance boundary: (a) Model A without seat; (b) Model B with seat.

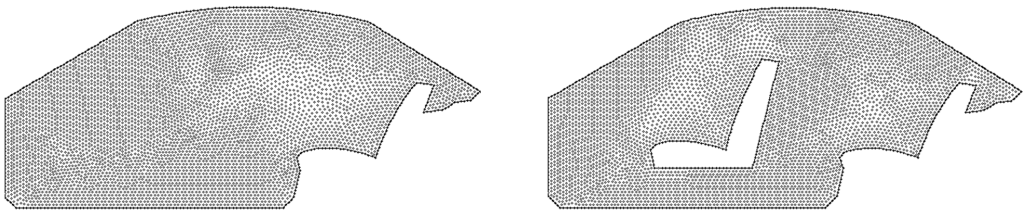

(a) Model A without seat (b) Model B with seat

Figure 8: Distributions of the LMFS nodes for (a) Model A without seat and (b) Model B with seat.

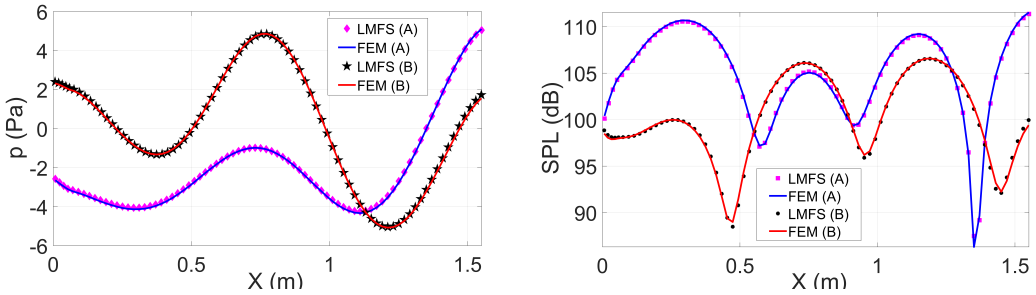

(a) Sound pressure (b) Sound pressure level

Figure 9: Numerical results of (a) sound pressure and (b) sound pressure level at the bottom boundary "ab" of car cavities without and with seat, under the frequency $f=400$Hz.

element method adopted the dense mesh (model A includes 689 boundary elements and 42,791 triangle elements, model B includes 792 boundary elements and 40,265 triangle elements). The proposed LMFS uses 11,534 nodes (model A) and 10,722 nodes (model B) as shown in Fig. 8. The number of supporting nodes in each local subdomain is set to be $m=15$.

In the case of impedance boundary conditions, we analyze and study the sound field of different models. Fig. 9 gives the comparisons of sound pressure and sound pressure level at the bottom boundary "ab" under different models with the frequency $f=400$Hz. We can see from Fig. 9 that the sound pressure of model A without seat is higher than that of model B with seat, while the sound pressure level of model A without seat is lower than that of model B with seat. This indicates that the simplified model can not well describe the practical problems. In addition, it can be observed that the LMFS solutions are in good agreement with the FEM solutions, demonstrating the accuracy and effectiveness of the present method.

Considering the car cavity with seat, Fig. 10 plots the distributions of sound pressure at low frequency $f=260$Hz and high frequency $f=500$Hz. It can be seen from Fig. 10 that the numerical results obtained by the proposed method is almost identical to the FEM. Moreover, the numerical results of LMFS is consistent with the FEM with more nodes

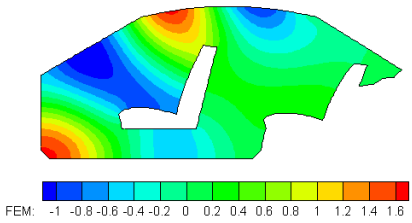

(a) FEM with $f=260$Hz

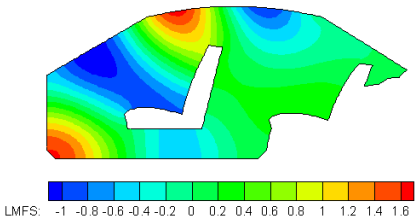

(b) LMFS with $f=260$Hz

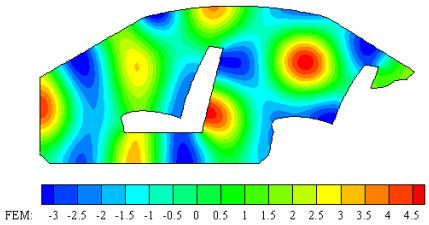

(c) FEM with $f=500$Hz

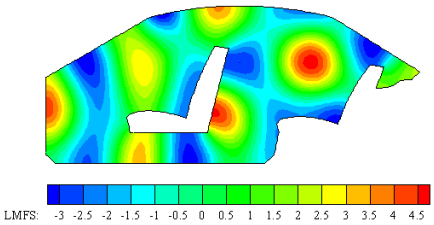

(d) LMFS with $f=500$Hz

Figure 10: Distributions of sound pressure inside the car cavity obtained by the FEM and LFMS under different frequencies.

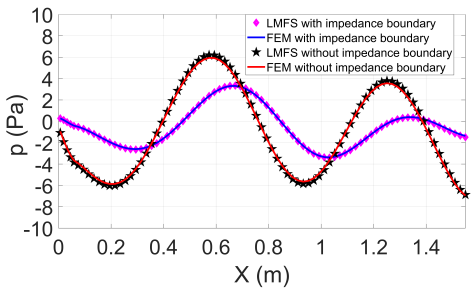

(a) Sound pressure

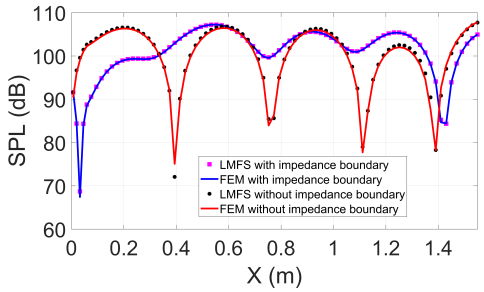

(b) Sound pressure level

Figure 11: Numerical results of (a) sound pressure and (b) sound pressure level at the bottom boundary "ab" of car cavities without and with impedance boundary condition, under the frequency $f=500$Hz.

even under high frequency excitation. It can be found that the developed method has better stability and reliability, and compared with FEM, LMFS has the advantage of not requiring meshing and saving data preparation time.

Next, we consider the cavities with and without impedance boundary condition. Numerical results under different boundary conditions with $f=500$Hz are depicted in Fig. 11. Noted that both the sound pressure and the sound pressure level inside the car cavity with impedance boundary condition is very different from the car cavity without impedance boundary condition. The maximum values of sound pressure and sound

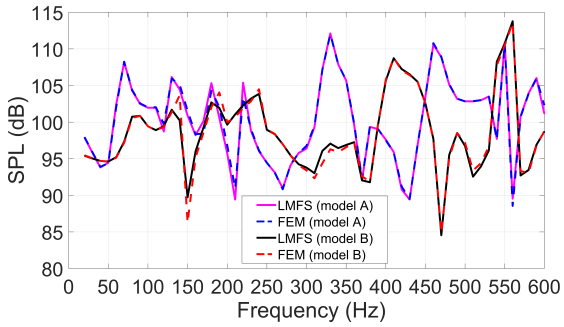

Figure 12: Acoustic frequency response at the monitoring point **F** obtained by LMFS and FEM.

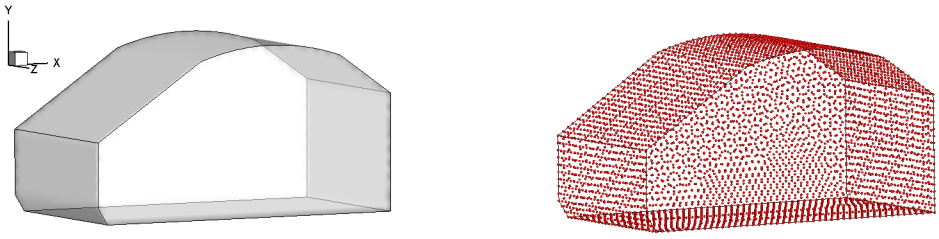

(a) Geometry model (b) Nodal distribution

Figure 13: (a) Geometry model of the problem and (b) the distribution of LMFS nodes.

pressure level of former are less than those of latter. Compared with the fully optimized FEM, it is found that LMFS also has certain accuracy and feasibility in solving acoustic problems under different boundary conditions.

Finally, we select the red monitoring point **F** (0.8m, 0.8m) in Fig. 7 to investigate the noise levels at the driver's ear position. Fig. 12 illustrates the sound pressure level at monitoring point for model A and B with respect to the frequency. It can be found from these frequency response curves that the satisfied results can be achieved by using the present method for different acoustic models.

4.3 Three-dimensional car cavity with impedance boundary

For the third example, we consider a simplified 3D car cavity (see Fig. 13(a)). The dimension of this sketch is 3.34m$\times$1.80m$\times$1.40m. The Neumann boundary condition with the vibration speed being 0.01m/s is imposed on the front of the car, and the Robin boundary condition is imposed on the top of the car. The physical parameter is consistent with that in Example 4.2.

As shown in Fig. 13(b), a total number of $N=27{,}470$ distributed nodes are discretized inside the whole computational domain, containing 15,404 boundary points. In the calcu-

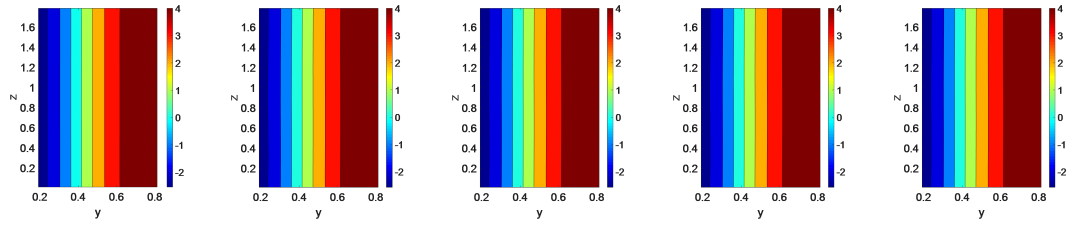

(a) FEM (b) $R_s=5$ (c) $R_s=10$ (d) $R_s=20$ (e) $R_s=30$

Figure 14: Comparison of numerical results on the front of the car obtained by using the FEM and the LMFS: (a) the FEM, (b) the LMFS with $R_s=5$, (c) the LMFS with $R_s=10$, (d) the LMFS with $R_s=20$, (e) the LMFS with $R_s=30$.

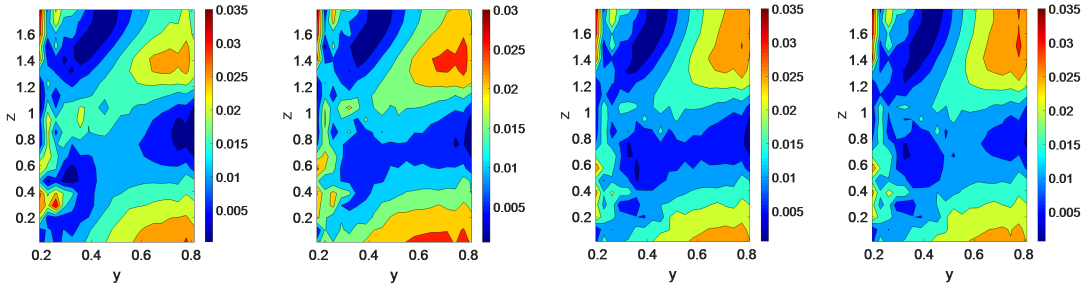

(a) $R_s=5$ (b) $R_s=10$ (c) $R_s=20$ (d) $R_s=30$

Figure 15: Absolute deviations between the FEM and the LMFS with different parameters of artificial radius: (a) $R_s=5$, (b) $R_s=10$, (c) $R_s=20$, (d) $R_s=30$.

lation, we set $m=80$. Firstly, we discuss the influence of the parameter R_S on the numerical accuracy in 3D problems. As shown in Fig. 14, the numerical results on the front of the car are in good agreement with the FEM results for various parameters ($R_S=5,10,20,30$). It can be found from Fig. 15 that the absolute deviations between the LMFS and the FEM remain basically unchanged for different values of R_S, indicating the accuracy and stability of the proposed LMFS for 3D cases. In the following calculation, $R_S=20$ is used for the sake of simplicity.

Then, we continue to set FEM with more nodes (includes 11,292 triangle elements and 141,528 tetrahedron elements) than the proposed method as the reference solution. It can be seen from Fig. 16 that the numerical results of LMFS, for both sound pressure and sound pressure level at the frequency $f=300$Hz, are consistent with the FEM. We can carefully conclude that the proposed method is sufficiently accurate in 3D car cavity problem when using fewer nodes compared with the FEM.

In addition, we obtain the frequency response curve at the monitoring point **F** (1.2m, 1.5m, 0.9m) in Fig. 13(a). Fig. 17 compares the numerical results obtained by the LMFS and FEM for frequencies changing from $f=20$Hz to $f=500$Hz. The results in Fig. 17 indicate that two methods agree well with each other, therefore, the developed method

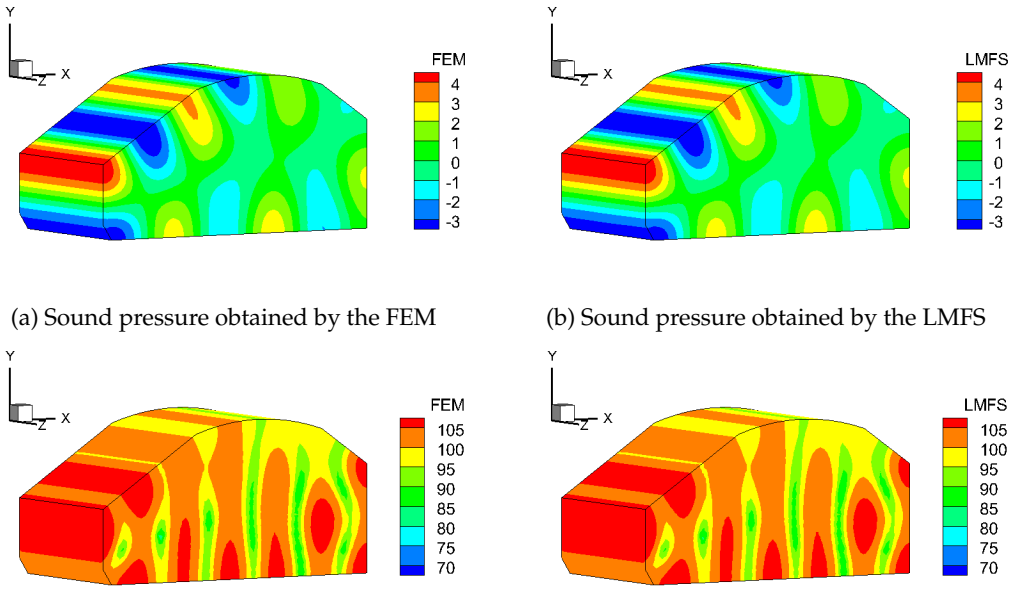

(a) Sound pressure obtained by the FEM

(b) Sound pressure obtained by the LMFS

(c) Sound pressure level obtained by the FEM

(d) Sound pressure level obtained by the LMFS

Figure 16: Contours of numerical results obtained by the FEM and LMFS under $f=300$Hz.

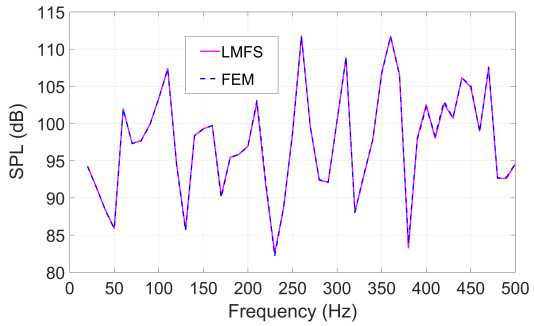

Figure 17: Acoustic frequency response at the monitoring point $\mathbf{F}$ obtained by the LMFS and FEM.

is also feasible and effective in 3D acoustic cavity problems with impedance boundary.

5 Conclusions

In this paper, the localized method of fundamental solutions (LMFS) is successfully extended to solve the acoustic field inside a car cavity with sound-absorbing materials. As a new local meshless method, the LMFS shows the following features in the acoustic anal-

ysis of car cavity: (a) the scheme is free from mesh generation and numerical integration and is a truly meshless method, which means that the time-consuming and troublesome pretreatment process is avoided; (b) the scheme is simple, accurate, and stable due to the use of fundamental solution of the physics equation; (c) the scheme is more convenient and straightforward for solving large-scale acoustic problems with complicated domains compared with existing boundary-type meshless methods, because of its localized characteristics.

Numerical experiments, including 2D and 3D benchmark examples, compared numerical results with the FEM solutions from COMSOL Multiphysics software, and confirm the effectiveness and performance of the developed method for the solution of car cavity acoustic problems with impedance conditions. Numerical results indicated that the present LMFS is an accurate, stable, convergent and efficient numerical algorithm. The method can be regarded as a competitive alternative to the standard method in the acoustic analysis of car cavity, especially for high-dimensional and large-scale problems. It should be noted that the present study focuses on the prediction of vehicle interior noise caused by the engine. The proposed scheme can not be directly used for external radiation/scattering acoustic field and structure-acoustic coupling analysis. For such problems, other auxiliary techniques, such as coupling strategy and domain truncation, should be introduced. This will be a key issue in our subsequent work.

Acknowledgements

The work described in this paper was supported by the National Natural Science Foundation of China (No. 11802151), the Natural Science Foundation of Shandong Province of China (No. ZR2019BA008).

References

[1] S. SINGH, AND A. R. MOHANTY, *HVAC noise control using natural materials to improve vehicle interior sound quality,* Appl. Acoust., 140 (2018), pp. 100–109.

[2] A. PURI, S. V. MODAK, AND K. GUPTA, *Global active noise control in vibro-acoustic cavities using acoustic sensing,* J. Sound Vibration, 455 (2019), pp. 256–274.

[3] A. ALONSO, J. PATRICIO, R. SUÁREZ, AND R. ESCANDÓN, *Acoustical retrofit of existing residential buildings: Requirements and recommendations for sound insulation between dwellings in Europe and other countries worldwide,* Building and Environment, 174 (2020), 106771.

[4] M. MEISSNER, *Application of modal expansion method for sound prediction in enclosed spaces subjected to boundary excitation,* J. Sound Vib., 500 (2021), 116041.

[5] C. R. WATTS, S. N. AWAN, AND Y. MARYN, *A comparison of cepstral peak prominence measures from two acoustic analysis programs,* J. Voice, 31 (2017), pp. 387.e381–387.e310.

[6] Y. XIAO, D. SHAO, H. ZHANG, C. SHUAI, AND Q. WANG, *An acoustic modeling of the three-dimensional annular segment cavity with various impedance boundary conditions,* Results Phys., 10 (2018), pp. 411–423.

[7] Z. J. FU, Q. XI, Y. D. LI, H. HUANG, AND T. RABCZUK, *Hybrid FEM-SBM solver for structural vibration induced underwater acoustic radiation in shallow marine environment,* Comput. Methods Appl. Mech. Eng., 369 (2020), 113236.
[8] M. AMDI, M. SOULI, J. HARGREAVES, AND F. ERCHIQUI, *Numerical investigation of a vibroacoustic analysis with different formulations,* Comput. Model. Eng. Sci., 85 (2012), pp. 329–346.
[9] F. IHLENBURG, Finite Element Analysis of Acoustic Scattering, Springer, 1998.
[10] Y. CHAI, W. LI, AND Z. LIU, *Analysis of transient wave propagation dynamics using the enriched finite element method with interpolation cover functions,* Appl. Math. Comput., 412 (2022), 126564.
[11] T. YOKOTA, S. SAKAMOTO, AND H. TACHIBANA, *Sound field simulation method by combining finite difference time domain calculation and multi-channel reproduction technique,* Acoust. Sci. Tech., 25 (2004), pp. 15–23.
[12] T. W. WU, Boundary Element Acoustics, Wit Press Southampton, (2000).
[13] J. T. CHEN, M. H. CHANG, K. H. CHEN, AND I. L. CHEN, *Boundary collocation method for acoustic eigenanalysis of three-dimensional cavities using radial basis function,* Comput. Mech., 29 (2002), pp. 392–408.
[14] L. CHEN, AND X. LI, *Meshless acoustic analysis using a weakly singular Burton-Miller boundary integral formulation,* Appl. Math. Mech., 41 (2020), pp. 1897–1914.
[15] F. J. WANG, Y. GU, W. Z. QU, AND C. Z. ZHANG, *Localized boundary knot method and its application to large-scale acoustic problems,* Comput. Methods Appl. Mech. Eng., 361 (2020), 112729.
[16] X. X. YUE, F. J. WANG, C. Z. ZHANG, AND H. X. ZHANG, *Localized boundary knot method for 3D inhomogeneous acoustic problems with complicated geometry,* Appl. Math. Model., 92 (2021), pp. 410–421.
[17] W. LI, Q. F. ZHANG, Q. GUI, AND Y. B. CHAI, *A coupled FE-Meshfree triangular element for acoustic radiation problems,* Int. J. Comput. Meth. Sing., 18 (2021), 2041002.
[18] G. FAIRWEATHER, AND A. KARAGEORGHIS, *The method of fundamental solutions for elliptic boundary value problems,* Adv. Comput. Math., 9 (1998), pp. 69–95.
[19] A. H. D. CHENG, AND Y. HONG, *An overview of the method of fundamental solutions-solvability, uniqueness, convergence, and stability,* Eng. Anal. Boundary Elements, 120 (2020), pp. 118–152.
[20] F. J. WANG, W. CAI, B. ZHENG, AND C. WANG, *Derivation and numerical validation of the fundamental solutions for constant and variable-order structural derivative advection-dispersion models,* Zeitschrift für angewandte Mathematik und Physik, 71 (2020), pp. 1–18.
[21] C. W. CHEN, C. M. FAN, D. L. YOUNG, K. MURUGESAN, AND C. C. TSAI, *Eigenanalysis for membranes with stringers using the methods of fundamental solutions and domain decomposition,* Comput. Model. Eng. Sci., 8 (2005), pp. 29–44.
[22] W. CHEN, AND M. TANAKA, *A meshless, integration-free, and boundary-only RBF technique,* Comput. Math. Appl., 43 (2002), pp. 379–391.
[23] B. JIN, AND Y. ZHENG, *Boundary knot method for some inverse problems associated with the Helmholtz equation,* Int. J. Numer. Methods Eng., 62 (2005), pp. 1636–1651.
[24] X. WEI, AND W. LUO, *2.5D singular boundary method for acoustic wave propagation,* Appl. Math. Lett., 112 (2021), 106760.
[25] Z. J. FU, W. CHEN, P. H. WEN, AND C. Z. ZHANG, *Singular boundary method for wave propagation analysis in periodic structures,* J. Sound Vibration, 425 (2018), pp. 170–188.
[26] P.-W. LI, *Space-time generalized finite difference nonlinear model for solving unsteady Burgers' equations,* Appl. Math. Lett., 114 (2021), 106896.
[27] W. Z. QU, AND H. HE, *A spatial-temporal GFDM with an additional condition for transient heat*

conduction analysis of FGMs, Appl. Math. Lett., 110 (2020), 106579.
[28] T. BELYTSCHKO, Y. Y. LU, AND L. GU, *Element-free Galerkin methods,* Int. Numer. Methods Eng., 37 (2010), pp. 229–256.
[29] X. L. LI, AND S. L. LI, *A linearized element-free Galerkin method for the complex Ginzburg-Landau equation,* Comput. Math. Appl., 90 (2021), pp. 135–147.
[30] L. WANG, *Radial basis functions methods for boundary value problems: Performance comparison,* Eng. Anal. Boundary Elements, 84 (2017), pp. 191–205.
[31] V. P. NGUYEN, T. RABCZUK, S. BORDAS, AND M. DUFLOT, *Meshless methods: A review and computer implementation aspects,* Math. Comput. Simul., 79 (2008), pp. 763–813.
[32] G. LIU, AND D. KARAMANLIDIS, *Mesh free methods: Moving beyond the finite eement method,* Appl. Mech. Rev., 56 (2003), pp. B17–B18.
[33] A. P. MARKOPOULOS, N. E. KARKALOS, AND E. L. PAPAZOGLOU, *Meshless methods for the simulation of machining and micro-machining: a review,* Arch. Comput. Methods Eng., 27 (2020), pp. 831–853.
[34] F. WANG, C. WANG, AND Z. CHEN, *Local knot method for 2D and 3D convection-diffusion-reaction equations in arbitrary domains,* Appl. Math. Lett., 105 (2020), 106308.
[35] X. X. YUE, F. J. WANG, P.-W. LI, AND C.-M. FAN, *Local non-singular knot method for large-scale computation of acoustic problems in complicated geometries,* Comput. Math. Appl., 84 (2021), pp. 128–143.
[36] Y.-C. LIU, C.-M. FAN, W. YEIH, C.-Y. KU, AND C.-L. CHU, *Numerical solutions of two-dimensional Laplace and biharmonic equations by the localized Trefftz method,* Comput. Math. Appl., 88 (2021), pp. 120–134.
[37] Q. XI, Z. FU, C. ZHANG, AND D. YIN, *An efficient localized Trefftz-based collocation scheme for heat conduction analysis in two kinds of heterogeneous materials under temperature loading,* Comput. Struct., 255 (2021), 106619.
[38] F. J. WANG, Z. T. CHEN, P.-W. LI, AND C.-M. FAN, *Localized singular boundary method for solving Laplace and Helmholtz equations in arbitrary 2D domains,* Eng. Anal. Boundary Elements, 129 (2021), pp. 82–92.
[39] F. J. WANG, Q. H. ZHAO, Z. T. CHEN, AND C.-M. FAN, *Localized Chebyshev collocation method for solving elliptic partial differential equations in arbitrary 2D domains,* Appl. Math. Comput., 397 (2021), 125903.
[40] C.-M. FAN, Y. K. HUANG, C. S. CHEN, AND S. R. KUO, *Localized method of fundamental solutions for solving two-dimensional Laplace and biharmonic equations,* Eng. Anal. Boundary Elements, 101 (2019), pp. 188–197.
[41] Y. GU, C.-M. FAN, W. Z. QU, AND F. J. WANG, *Localized method of fundamental solutions for large-scale modelling of three-dimensional anisotropic heat conduction problems-Theory and MATLAB code,* Comput. Struct., 220 (2019), pp. 144–155.
[42] F. J. WANG, C.-M. FAN, Q. S. HUA, AND Y. GU, *Localized MFS for the inverse Cauchy problems of two-dimensional Laplace and biharmonic equations,* Appl. Math. Comput., 364 (2020), 124658.
[43] F. WANG, C.-M. FAN, C. ZHANG, AND J. LIN, *A localized space-time method of fundamental solutions for diffusion and convection-diffusion problems,* Adv. Appl. Math. Mech., 12 (2020), pp. 940–958.
[44] W. W. LI, *Localized method of fundamental solutions for 2D harmonic elastic wave problems,* Appl. Math. Lett., 112 (2021), 106759.
[45] Y. GU, C.-M. FAN, AND Z. J. FU, *Localized method of fundamental solutions for three-dimensional elasticity problems: theory,* Adv. Appl. Math. Mech., (2021), doi: 10.4208/aamm.OA-2020-134.
[46] W. Z. QU, C.-M. FAN, Y. GU, AND F. J. WANG, *Analysis of three-dimensional interior acoustic*

fields by using the localized method of fundamental solutions, Appl. Math. Model., 76 (2019), pp. 122–132.

[47] W. Z. Qu, C.-M. Fan, and Y. Gu, *Localized method of fundamental solutions for interior Helmholtz problems with high wave number,* Eng. Anal. Boundary Elements, 107 (2019), pp. 25–32.

[48] Y. Gu, C.-M. Fan, W. Z. Qu, F. J. Wang, and C. Z. Zhang, *Localized method of fundamental solutions for three-dimensional inhomogeneous elliptic problems: theory and MATLAB code,* Comput. Mech., 64 (2019), pp. 1567–1588.

[49] T. Belytschko, Y. Krongauz, D. Organ, M. Fleming, and P. Krysl, *Meshless methods: An overview and recent developments,* Comput. Methods Appl. Mech. Eng., 139 (1996), pp. 3–47.

[50] A. Chaigne, Structural Acoustics and Vibrations, Springer, New York, 2007.

[51] M. Kassem, C. Soize, and L. Gagliardini, *Structural partitioning of complex structures in the medium-frequency range, An application to an automotive vehicle,* J. Sound Vib., 330 (2011), pp. 937–946.

[52] G. Wang, *The research of computational method for vehicle body structure vibration and noise based on nodal integration,* Hunan: Hunan University, 2016.

[53] Z. T. Chen, and F. J. Wang, *On the supporting nodes in the localized method of fundamental solutions for 2D potential problems with Dirichlet boundary condition,* AIMS Math., 6 (2021), pp. 7056–7069.

[54] Z. J. Fu, Z. Y. Xie, S. Y. Ji, C. C. Tsai, and A. L. Li, *Meshless generalized finite difference method for water wave interactions with multiple-bottom-seated-cylinder-array structures,* Ocean Eng., 195 (2020), 106736.